Effects of film thickness and contact load on nanotribological properties of sputtered amorphous carbon thin films

X. G. Ma, D. J. Wan, K. Komvopoulos*, and D. B. Bogy
Department of Mechanical Engineering, University of California, Berkeley, California 94720, USA
Y.-S. Kim
School of Advanced Materials Engineering, Kookmin University, Seoul 136-702, South Korea

ABSTRACT

The nanoscale friction properties of amorphous carbon films of thicknesses in the range of 5-85 nm sputtered on Si(100) substrates were investigated with a surface force microscope using a Berkovich diamond tip of nominal radius equal to ~200 nm and normal contact loads between 10 and 1200 μN. The dependence of friction properties on normal load and film thickness was studied in terms of the nanomechanical properties of the carbon films, images of the scratched film surfaces and scratch grooves, and using results from a previous analytical friction model. It is shown that at the onset of scratching the coefficient of friction decreases with increasing normal load to a minimum value (transition load), and then increases with normal load to a maximum value, after which, it either remains constant or decreases slightly with further increase of the normal load. The dominant friction mechanism in the low-load range is adhesion, while both adhesion and plowing friction mechanisms contribute to the friction behavior in the intermediate- and high-load ranges. Thinner films yielded higher friction coefficients than thicker films for normal loads less than 50 μN (low-load range), while thinner films exhibited lower friction coefficients for normal loads greater than 150 μN (high-load range). The lower load-bearing capacity, effective hardness (strength) of thinner films, and dominant friction mechanisms in each load range provide insight into the dependence of the coefficient of friction on the film thickness and normal load.

1. INTRODUCTION

Amorphous carbon (a-C) films are characterized by excellent friction properties [1], high hardness, superior substrate adhesion [2], high thermal conductivity, low dielectric constant, and high optical transparency in the infrared wavelength range[3]. Because of these attractive properties, a-C films are used in various optical, electrical, and tribological systems. In particular, thin a-C films are used as hard protective overcoats in magnetic rigid disk drives [4,5]. Ultrathin carbon films with high wear and corrosion resistance are of profound importance to high-density magnetic recording [6]. Demands for higher storage densities have necessitated continual decrease of the carbon overcoat thickness and distance between the slider and the disk surface. Such low spacing promotes intermittent contact between the slider and the disk, possibly resulting in damage of the disk and slider surfaces [7]. Consequently, the tribological properties of thin carbon overcoats are of great importance to magnetic storage. Over the past decades, numerous studies have been performed on the wear resistance, friction, and adhesion of ultrathin carbon films.

Nano-/microtribology plays an important role in many emerging fields, such as high-density magnetic recording and microelectromechanical systems. Because of the small size and mass of the elements used in such small systems, microsystem dynamic performance greatly depends on surface properties [8]. Therefore, it is essential to investigate the factors affecting the friction behavior of miniature elements at such small scales. Hardness and elastic modulus of carbon films characterize the relation between their mechanical and friction properties [3]. While the coefficient of friction is known to be independent of normal load in the high-load range, load-dependent friction behavior has been often observed in the nanoscale [3,9]. Film thickness, internal stress, and plastic deformation in layered media have been also found to affect the friction response [2,10].

In spite of many published works related to the nanotribological properties of thin carbon films, the effect of film thickness on the friction behavior and surface damage of thin-film media (especially ultrathin films) subjected to light contact loads (<1 mN) has received relatively little attention. It is not clear how the friction mechanisms and surface damage modes change with film thickness and contact load, especially very light loads of the order of μN. Thus, the objectives of this study were to investigate the low-load friction behavior of a-C films with thicknesses in the range of 5-85 nm sputtered on Si(100) substrates. Friction force measurements were obtained with a surface force microscope (SFM) comprising an atomic force microscope (AFM) equipped with a highly sensitive force-displacement transducer, capable of applying and sensing normal and tangential forces in a controlled fashion. To investigate the effects of normal load, hardness, film thickness, and plastic deformation of the silicon substrate on the film friction behavior, scratch tests were performed with a sharp diamond tip attached to the transducer, using ramp loading to a peak load of 1200 μN. The scratched surfaces and residual depth of scratch grooves were studied with the SFM operated at light contact loads. Results are presented to elucidate the effects of film thickness and normal load on the nanoscale friction behavior and surface damage modes of thin a-C films.

2. EXPERIMENTAL PROCEDURES

2.1. Specimens

Thin a-C films were deposited on Si(100) substrates using a commercial radio frequency (RF) sputtering system (Perkin-Elmer, Randex 2400 model). To obtain films with different mechanical properties, the depositions were performed under conditions of working pressure p = 3 mTorr, argon gas flow rate f = 20 sccm, deposition time t = 3 min, substrate bias voltage V_b = -200 V, and RF power P = 200 to 750 W. In addition, to obtain films with similar mechanical properties and different thickness, depositions were performed at P = 750 W, p = 3 mTorr, f =

20 sccm, V_b = -200 V, and $3\,\text{min} \le t \le 9\,\text{min}$. The film thickness h was obtained from cross-section transmission electron microscopy images. Under the above deposition conditions, carbon films of thickness in the range of 5-85 nm and root-mean-square (rms) surface roughness σ between 0.075 and 0.088 nm were synthesized on smooth Si(100) surfaces of rms roughness equal to ~0.2 nm. Surface roughness measurements were obtained from 1 μm x 1 μm SFM surface area images using a diamond tip of nominal radius equal to 90 nm under a contact force of 1.5 μN. Table 1 gives the thickness, roughness, and mechanical properties of the investigated a-C films in terms of deposition conditions.

2.2. Nanoindentation Experiments

The nanomechanical properties of the sputtered a-C films were evaluated using an SFM comprising an AFM interfaced with a surface force transducer (Triboscope, Hysitron Inc.). The capacitive force-displacement transducer replaces the original cantilever of the AFM, and is interfaced with a detector assembly, signal adapter, and a controller with dedicated software. Details of the SFM instrument are given elsewhere [6]. Nanoindentation experiments were performed with a cube-corner diamond tip with a nominal radius of curvature equal to 90 nm and loading/unloading times both equal to 5 s. Tuning of the electrostatic force constant of the transducer and tip-shape calibration were carried out before testing. The method of Oliver and Pharr [11] was used to perform tip calibrations. Indentations of different contact depths were produced on fused quartz of hardness and elastic modulus approximately equal to 10 and 73 GPa, respectively, in order to determine the tip-shape function. The hardness and elastic modulus of the films were calculated using the contact depth at maximum load and the slope of the unloading portion of the force-displacement curve, respectively. Additional information about the tip shape calibration method and procedures of the nanoindentation experiment can be found in Refs. [6] and [11].

2.3. Nanoscratch Experiments

Nanoscratch tests were carried out with the same system as used in the nanoindentation tests. A Berkovich diamond tip of nominal radius of curvature equal to ~200 nm was used for scratching. The normal force and sliding speed were varied in the ranges of 10-1200 μN and 0.025-0.2 μm/s, respectively, and the scratch distance of the tip was fixed at 2 μm. Before each scratch test, the film surfaces were cleaned with acetone and scanned at a light contact force of 1.5 μN using a scan frequency of 1 Hz to obtain the images of the original film surfaces. Figure 1 shows typical load-unload and displacement curves of the diamond tip during a nanoscratch test. Each scratch test consisted of five sequential steps: (1) tip advancement by 1 μm under a contact force of 1.5 μN after engagement with the film surface; (2) stabilization of the transducer for 5 s to allow the controller to keep up with the tip movement under normal force equal to 1.5 μN; (3) tip movement by 2 μm over a specific time under contact force linearly increasing from 1.5 μN to the set maximum value; (4) load decrease (unloading) after scratching to 1.5 μN in 5 s; and (5) tip retraction to its original engagement position under a normal force equal to 1.5 μN. The distance between each scratch test was set equal to or larger than 1 μm to avoid interaction between neighboring scratches. A total of 300 data sets of normal and lateral force and displacement were recorded during each scratch test. The coefficient of friction was obtained while the tip was scratching the film surface. After each scratch test, the surface area containing the scratch groove was imaged again by the same tip under a contact force of 1.5 μN to obtain SFM images of the scratched surfaces.

3. RESULTS

Nanoindentation results for the a-C films are given in Table 1. Assuming proportionality between material hardness and yield strength and same Poisson ratio for the film and substrate

materials, the film hardness H_f was calculated from the measured effective hardness H_{eff} using the following equation that accounts for the substrate effect [12],

$$H_f = H_{eff} \cdot \left\{ \frac{H_s}{H_{eff}} + \left(1 - \frac{H_s}{H_{eff}}\right) \exp\left[\left(\frac{d_c}{h}\right)\left(\frac{E_s}{E_f}\right)^{1/2} \right] \right\} \quad (1)$$

where d_c is the indentation depth, E is the elastic modulus, and H is the hardness. Subscripts s and f denote substrate and film materials, respectively. The elastic modulus ratio E_s/E_f in Eq. (1) can be approximated as [13]

$$\frac{E_s}{E_f} \approx \left\{ \frac{\left[\left(1-\nu^2\right)/E\right]_{eff}}{\left(1-\nu_s^2\right)/E_s} - e^{-\alpha h/d_c\sqrt{\pi}} \right\} \left(1 - e^{-\alpha h/d_c\sqrt{\pi}}\right)^{-1} \quad (2)$$

where α is a numerical factor that depends on the ratio a/h, where a is the square root of the projected indentation area. Values of α were obtained from a plot of α versus a/h for a circular contact [13].

Typical plots of the coefficient of friction versus normal load are shown in Figs. 2-6 for five different film thickness values. Each figure also contains SFM images of the scratched surface and the residual depth profile of the corresponding scratch groove. All films show similar friction coefficient variations with normal load. Three regimes can be identified in each figure (designated as I, II, and III). In regime I, the friction coefficient decreases with normal load to a minimum value. Hereafter, the load corresponding to the minimum coefficient of friction will be referred to as the *transition load* and will be designated as point A in the following figures. In regime II, the friction coefficient increases with normal load to a maximum value (point B in all figures), while in regime III, it either reaches a steady state or decreases slightly with further increases of the normal load. The normal load corresponding to the maximum coefficient of friction increases with the film thickness.

The scratch morphologies of all specimens exhibit similarities. The cross-sectional area of each scratch is approximately triangular and increases with normal load. The asymmetry of the scratch groove is evidently caused by the asymmetry of the Berkovich tip shape relative to the scratch direction. Surface damage on the film surfaces was not observed for loads less than the transition load (point A). This is evidenced from the residual scratch depth profiles. Between points A and B, the scratch depth increases with normal load, exhibiting a relatively smooth bottom surface topography. After point B, the roughness at the bottom of the groove increases with normal load, suggesting the occurrence of fine wear debris and, possibly, a wear process involving discontinuous material removal. The three ranges of friction coefficient and associated residual depth profiles correspond to different friction mechanisms, which are discussed in the following section.

Figure 7 shows the variation of the coefficient of friction of a 5.6 nm thick a-C film with contact load. After the transition load (point A), the coefficient of friction increases with normal load in regime II; however, at a load of ~37 μN, the coefficient of friction increases abruptly. This might be an indication of rapid cracking or delamination in the film. Hereafter, the load associated with the abrupt increase of the friction coefficient will be referred to as the *critical load* [14]. The coefficient of friction plots for film thickness of 10.9 and 15.6 nm and higher normal loads also reveal a similar sharp increase at corresponding critical loads (Fig. 8). When the normal load exceeds the critical load, the coefficient of friction increases abruptly from 0.2-0.25 to about 0.35–0.5. The critical load for 10.9 and 15.6 nm thick films is equal to 640 and 890 μN, respectively. Similar trends have been reported in other studies [15]. The SFM surface images and the residual depth profiles indicate the formation of wear particles and possible peeling-off of the films for normal loads close to the critical load. The thicker the film, the higher the critical load. For films thicker than 28 nm, critical loads could not be obtained because the required normal force was above the capacity of the force transducer.

Figure 9 shows the variation of the coefficient of friction for films of different thickness as a function of normal load. For light loads less than 50 μN, higher friction coefficient values were obtained with thinner films. The trend is clear among the thinner films with thickness less than 15.6 nm, while no significant film-thickness dependence of the friction coefficient is observed among the thicker films (i.e., thickness greater than 28 nm). For loads greater than 150 μN, an opposite trend is shown, i.e., lower coefficient of friction values are produced for thinner films than thicker films. Again, thicker films do not reveal a clear film thickness dependence of the coefficient of friction.

4. DISCUSSION

The plots of the coefficient of friction versus normal load demonstrate the existence of three distinct regimes. The coefficient of friction decreases with increasing normal load in regime I to a minimum value corresponding to the transition load (point A), then increases with load (regime II) reaching a peak value (point B), and thereafter it either decreases or remains constant with increasing normal load (regime III). Friction between two sliding surfaces is a manifestation of various simultaneous effects, including adhesion due to the formation of asperity junctions, deformation and fracture of asperities due to mechanical interlocking (roughness effect), and plowing by hard asperities or wear particles trapped at the contact interface. Since the roughness of the tested a-C films was similar, the differences in the coefficient of friction results are most likely due to different contributions of the adhesion and plowing mechanisms. Therefore the friction coefficient μ can be expressed as

$$\mu = \mu_a + \mu_p \tag{3}$$

where μ_a and μ_p denote adhesion and plowing friction components, respectively. The adhesion friction component can be obtained as

$$\mu_a = \frac{A\tau}{L} \tag{4}$$

where A is the real contact area, τ is the average shear strength at the contact interface, and L is the normal load. For elastic deformation of spherical asperities, the contact area is given by [16],

$$A = \pi\left(\frac{3LR}{4E^*}\right)^{2/3} \tag{5}$$

where E^* is the effective elastic modulus given by $E^* = \left[\left(1-\nu_1^2\right)/E_1 + \left(1-\nu_2^2\right)/E_2\right]^{-1}$, and R is the effective radius of curvature given by $R = \left[1/R_1 + 1/R_2\right]^{-1}$, where subscripts 1 and 2 denote the two contacting surfaces. Substituting Eq. (5) into Eq. (4), we can write the adhesion component of friction for purely elastic asperity microcontacts as

$$\mu_a = \pi\,\tau\left(\frac{3R}{4E^*}\right)^{2/3} L^{-1/3} \tag{6}$$

Equation (6) indicates a linear dependence of μ_a on $L^{-1/3}$. Figure 10 shows the variation of the coefficient of friction with normal load during the initial stage of scratching (regime I). The linear relation between μ_a and $L^{-1/3}$ observed for all the films suggests that the principal friction mechanism in the light-load range is adhesion. Studies have demonstrated that the friction coefficient decreases with normal load when adhesion is predominant and increases with normal load when plowing prevails [17,18]. Wang and Kato [19] identified two scratching regimes of no plastic deformation and plastic deformation, and reported an important role of adhesion in the first regime. The SFM images shown in Figs. 2-7 do not provide evidence of plastic deformation at the film surface during the initial stage of scratching (regime I), suggesting that adhesion is the dominant mechanism in this regime.

For normal loads greater than the transition load, residual grooves were observed on the scratched film surfaces and the coefficient of friction increased with normal load (regime II). In

this regime, surface damage of the films is due to plastic deformation and depends on the film hardness. Figure 11 shows the dependence of the transition load on the film hardness and thickness. The transition load increases monotonically with film hardness, supporting the view that plastic flow is the principal deformation mode in regime II. When plastic deformation at and below the contact region commences, plowing and adhesion mechanisms control the magnitude of the friction force. A friction model that accounts for both plowing and adhesion effects and plastic contact conditions [20] was used to characterize the friction in regime II. In this model, a rigid conical wear particle (or asperity) with a hemispherical tip penetrates and plows through a softer surface. When the penetration depth is shallow, plowing occurs only by the spherical tip and the friction coefficient is given by [20]

$$\mu = \frac{2}{\pi}\left[1-\left(1-\frac{d}{r}\right)^2\right]^{-1}\left[\cos^{-1}\left(1-\frac{d}{r}\right)-\left(1-\frac{d}{r}\right)\left\{1-\left(1-\frac{d}{r}\right)^2\right\}^{1/2}+\frac{K^n}{3}\left(\frac{s}{k_f}\right)\left(\frac{d}{r}\right)\right] \qquad (7)$$

where d is the penetration depth, r is the tip radius of curvature, K is a material strain constant, n is the strain hardening coefficient, s is the interfacial shear strength, and k_f is the shear strength of the plowed material (film). In the present study, the tip radius was ~200 nm and the penetration depth in regime II was less than 30 nm, i.e., much smaller than the tip radius. Hence, it is appropriate to assume a spherical tip and use Eq. (7) to analyze the results of regime II. Experimental and analytical friction coefficient results are contrasted in Fig. 12. The analytical results were obtained for $s/k_f = 0.8$, which is a reasonable value for unlubricated sliding, and n = 0.02 since strain hardening of the films is insignificant [20]. The fair agreement between analytical and experimental friction data suggests that plowing and adhesion are the dominant friction mechanisms in regime II. In this regime, the tip plows through the film material producing a relatively smooth groove surface, as evidenced from the groove profiles

shown in Fig. 2-7. The relatively smooth residual depth profile and few wear particles along the groove suggest that microfracture did not occur [21-23].

The friction coefficient in regime III was either constant or decreased marginally. Residual depth profiles of scratched film surfaces from regime III revealed irregularities and increased roughness at the bottom of the grooves, suggesting the formation of fine wear debris. It is also possible that microfracture was another contributing mechanism in regime III. The onset of regime III at penetration depths close to the film thickness (e.g., 10.9 and 15.6 nm thick films) suggests that the relatively severe damage in this friction regime commences when the tip reaches the film/substrate interface. It is possible that at this juncture delamination of the film might have occurred due to excessive plastic flow in the substrate, yielding large strain gradients at the interface. When plastic deformation in the substrate reaches a critical state, delamination or fracture of the film may occur due to the strain mismatch at the film/substrate interface. Evidently, this failure process depends on the film thickness since higher normal loads are required for thicker films in order to produce such excessive subsurface plasticity.

In the low-load range (normal load <50 μN), thinner films yielded higher friction coefficients than thicker films. This may be attributed to the greater effect of the plowing friction mechanism resulting from the greater penetration depth in the case of thinner films subjected to the same normal load. The lower load-carrying capacity of thinner films enhances plastic flow in the substrate, thereby leading to higher friction. Contrary to the low-load range, thinner films exhibited lower coefficients of friction in the high-load range (normal load >150 μN). Since plowing is the major friction mechanism at higher loads (regimes II and III), if the tip plows through both the film and the substrate, a lower friction force would be expected for thin films and low film hardness. Figure 9 shows that the 10.9 and 15.6 nm thick films yielded low coefficients of friction, especially the 10.9 nm thick film. The fact that both these films and corresponding substrates were plowed during scratching and thicker films of thickness equal to

28.7, 46, and 85 nm possess similar hardness is direct evidence for the thickness dependence of the friction coefficient in the high-load range.

5. CONCLUSIONS

The nanoscale friction properties of amorphous carbon films with thickness in the range of 5-85 nm sputtered on Si(100) substrates were investigated by performing nanoscratch tests with a surface force microscope using a Berkovich tip of nominal radius of curvature equal to ~200 nm and contact loads in the range of 10-1200 μN. The dependence of the film friction behavior on normal load and film thickness was analyzed in the context of experimental results for the nanomechanical properties of the films, SFM images of the scratched film surfaces and nanotopographies of the produced plowing grooves, and analytical results from a previous friction model. Based on the presented results and discussion, the following main conclusions can be drawn.

(1) The coefficient of friction curves of all films demonstrated the existence of three regimes characterized by different load ranges, depending on film thickness. The coefficient of friction decreased initially with increasing contact load to a minimum value (transition load) corresponding to the initiation of scratching (regime I), subsequently it increased to a maximum value (regime II), and then it either remained constant or decreased slightly with further increasing the normal load (regime III).

(2) The dominant friction mechanism in regime I is adhesion, while both adhesion and plowing contribute to the coefficient of friction in regimes II and III. The friction coefficient results for regime II are in fair agreement with analytical results for a hemispherical tip plowing through a softer surface. The load range for regime II increases with film thickness.

(3) Relatively thinner films exhibited higher coefficients of friction than thicker films in the low-load range (normal load <50 μN). Alternatively, lower friction coefficients were obtained with thinner films in the high-load range (normal load >150 μN) than with thicker films.

(4) The lower load-bearing capacity and lower hardness (strength) of thinner films and the identified dominant friction mechanisms in each load range yield insight into the dependence of the coefficient of friction of the films on normal load and film thickness.

ACKNOWLEDGMENTS

This research was supported by the Computer Mechanics Laboratory at the University of California at Berkeley. The fellowship to the last author through a Korea Research Foundation Grant (KRF-2001-013-E00106) is also gratefully acknowledged.

REFERENCES

[1] D. B. Bogy, X. Yun, B. J. Knapp, Enhancement of head-disk interface durability by use of diamond-like carbon overcoats on the slider's rails, IEEE Transactions on Magnetics 30 (2) Part: 1-2 (1994) 369 –374.

[2] Y. Xie, R. J. Llewellyn, D. Stiles, Amorphous diamond coating of tungsten carbide and titanium carbonitride for erosive slurry pump component service, Wear 250 (2001) 88-99.

[3] V. Prabhakaran, F. E. Talke, Wear and hardness of carbon overcoats on magnetic recording sliders, Wear 243 (2000) 18–24.

[4] C.-J. Lu, D. B. Bogy, S. S. Rosenblum, G. J. Tessmer, Nano-tribological investigations of carbon overcoats: Correlation with Raman spectra, Thin Solid Films 268 (1-2) (1995) 83-90.

[5] D. B. Bogy, X. Yun, Enhancement of head-disk interface durability by use of diamond-like carbon overcoats on the slider rails, IEEE Trans. Magn. 30 (2) (1994) 369–374.

[6] W. Lu, K. Komvopoulos, Nanotribological and nanomechanical properties of ultrathin amorphous carbon thin films synthesized by reactive radio frequency sputtering, J. Tribol. 123 (2001) 641-650.

[7] L.-Y. Huang, K.-W. Xu, K.-W. Lu, B. Guelorget, Analysis of nano-scratch behavior of diamond-like carbon films, Surf. Coat. Technol. 154 (2002) 232– 236.

[8] T. Yokohata, K. Kato, T. Miyamoto, R. Kaneko, Load-dependency of friction coefficient between silicon-oxides and diamond under ultra-low contact load, J. Tribol. 120 (1998) 503-509.

[9] D. F. Wang, K. Kato, Effect of coating thickness on friction for carbon nitride films in repeated sliding against a spherical diamond with nano-scale asperities, Wear 252 (2002) 210-219.

[10] W.-J. Wu, M.-H. Hon, The effect of residual stress on adhesion of silicon-containing diamond-like carbon coatings, Thin Solid Films 345 (1999) 200-207.

[11] W. C. Oliver, G. M. Pharr, An improved technique for determining hardness and elastic modulus using load and displacement sensing indentation experiments, J. Mater. Res. 7 (6) (1992) 1564–1583.

[12] A. K. Bhattacharya, W. D. Nix, Analysis of Elastic and Plastic Deformation Associated With Indentation Testing of Thin Films on Substrates, Int. J. Solids Struct. 24 (1988) 1287–1298.

[13] R. B. King, Elastic Analysis of Some Punch Problems for a Layered Medium, Int. J. Solids Struct. 23 (1987) 1657–1664.

[14] R. Bunshah, *Handbook of Hard Coatings: Deposition Technologies, Properties and Applications*, William Andrew Publishing, 2001.

[15] H. Deng, T. Scharf, J. Barnard, Adhesion assessment of silicon carbide, carbon, and carbon nitride ultrathin overcoats by nanoscratch techniques, J. Appl. Phys. 81 (8) (1997) 5396-5398.

[16] K. L. Johnson, *Contact Mechanics*, Cambridge Univ. Press, Cambridge, U.K., 1985.

[17] J. Malzbender, G. de With, Analysis of scratch testing of organic-inorganic coatings on glass, Thin Solid Films 386 (1) (2001) 68-78.

[18] J. Malzbender, G. de With, Scratch testing of hybrid coatings on float glass, Surf. Coat. Technol. 135 (2-3) (2001) 202-207.

[19] D. F. Wang, K. Kato, Friction studies of ion beam assisted carbon nitride coating sliding against diamond pin in water vapor, Wear 217 (1998) 307-311.

[20] K. Komvopoulos, Sliding friction mechanisms of boundary-lubricated layered surface: Part II - Theoretical analysis, Tribology Transactions 34 (2) (1991) 281-291.

[21] M. Bai, K. Kato, N. Umehara, Y. Miyake, J. Xu, H. Tokisue, Scratch-wear resistance of nanoscale super thin carbon nitride overcoat evaluated by AFM with a diamond tip, Surf. Coat. Technol. 126 (2-3) (2000) 181-194.

[22] C. Charitidis, S. Logothetidis, M. Gioti, A comparative study of the nanoscratching behavior of amorphous carbon films grown under various deposition conditions, Surf. Coat. Technol. 125 (2000) 201–206.

[23] K. F. Chan, C. W. Ong, C. L. Choy, Nanoscratch characterization of dual-ion-beam deposited C-doped boron nitride films, J. Vac. Sci. Technol. A17 (6) (1999) 3351-3357.

Table 1. Thickness, rms roughness, and mechanical properties of a-C films versus deposition conditions.[c] (h_c is the contact depth at which the hardness values were obtained.)

P (W)	t (min)	h (nm)	σ (nm)	H_{eff} (GPa)	H_f (GPa)	h_c/h	E_r (GPa)
200 [a]	3	5.6	0.081	13.41	17.19	0.52	158.49
300 [a]	3	10.9	0.075	14.89	17.11	0.31	143.27
400 [a]	3	15.6	0.082	18.25	19.83	0.22	151.67
750 [b]	3	28.7	0.079	34.74	39.19	0.20	165.67
750 [b]	5	46	0.088	39.18	42.45	0.13	168.55
750 [b]	9	85	0.086	36.05	37.84	0.08	181.50

[a]90 nm tip radius.
[b]30 nm tip radius.
[c]f = 20 sccm, p = 3 mTorr; V_b = –200 V.

List of Figures

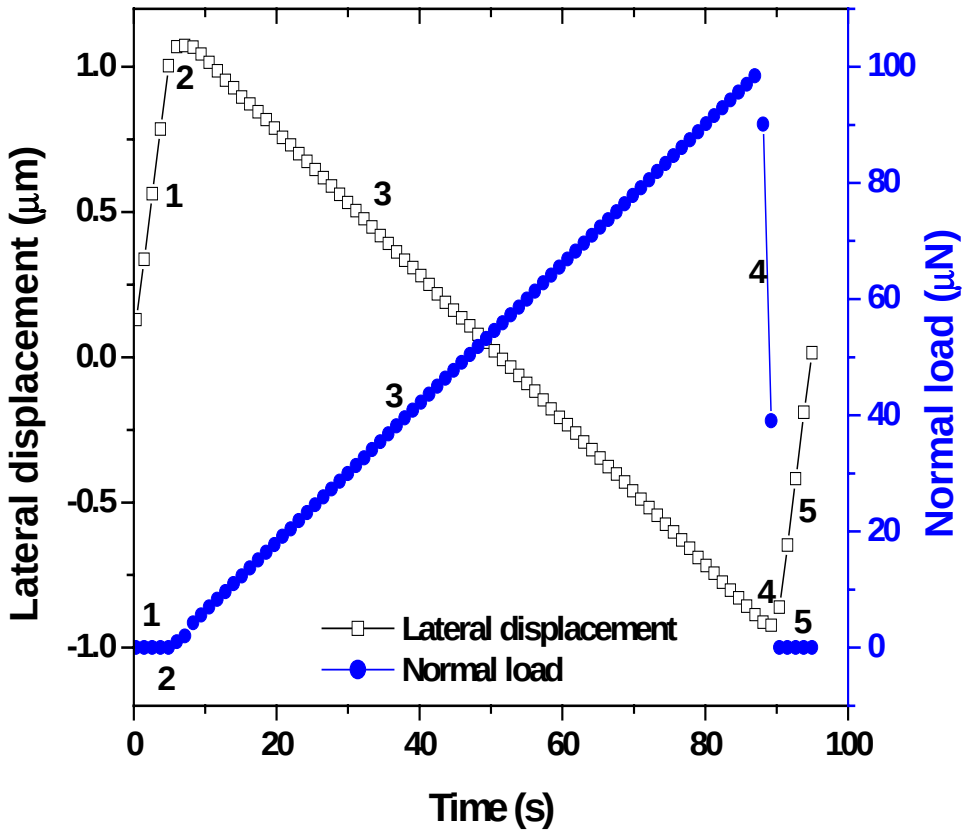

Fig. 1. Typical load, unload, and lateral displacement curves for scratch testing.

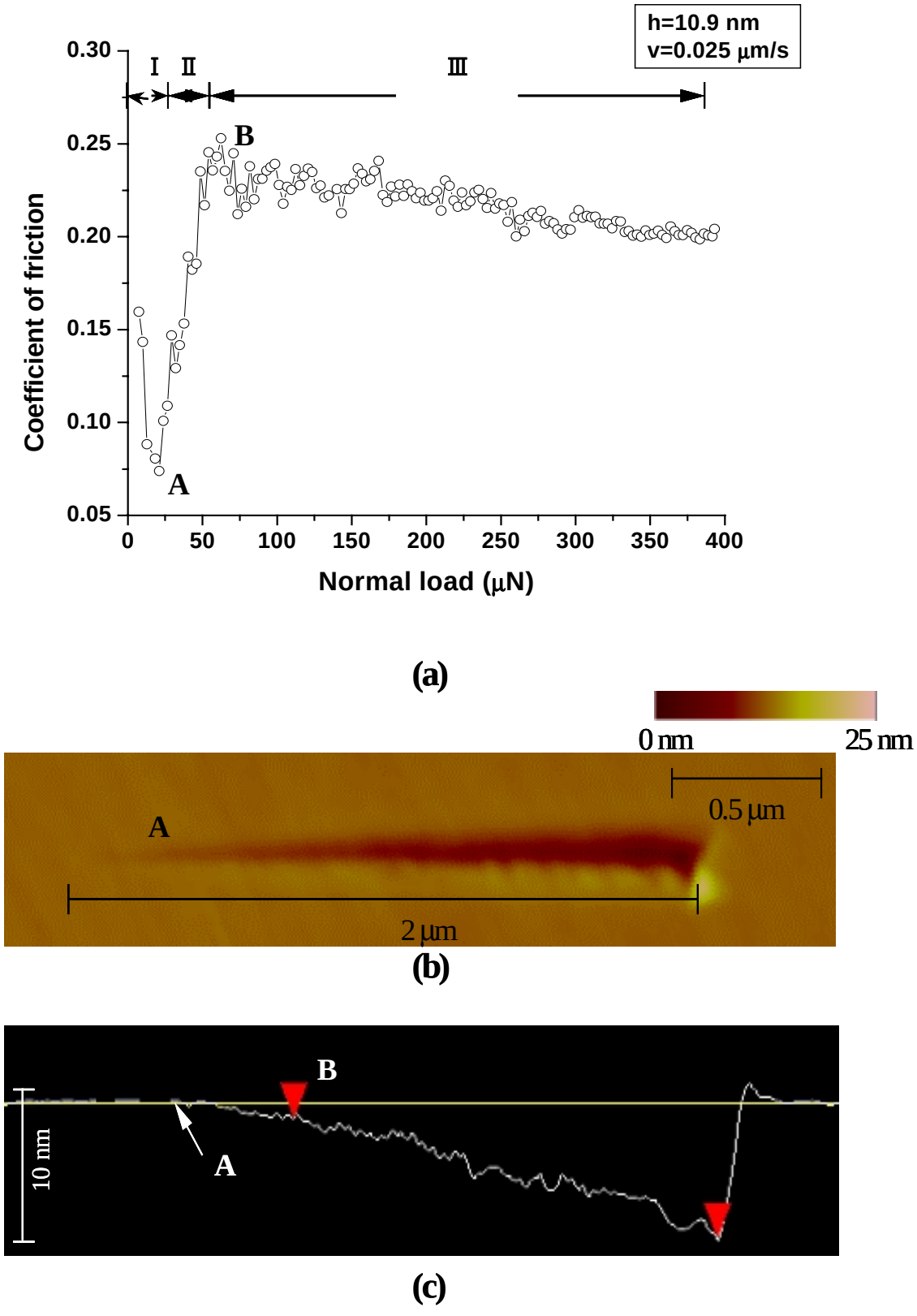

Fig. 2. (a) Friction coefficient versus normal load for 10.9 nm thick film, (b) SFM image of scratched film surface, and (c) cross-sectional view of residual depth profile.

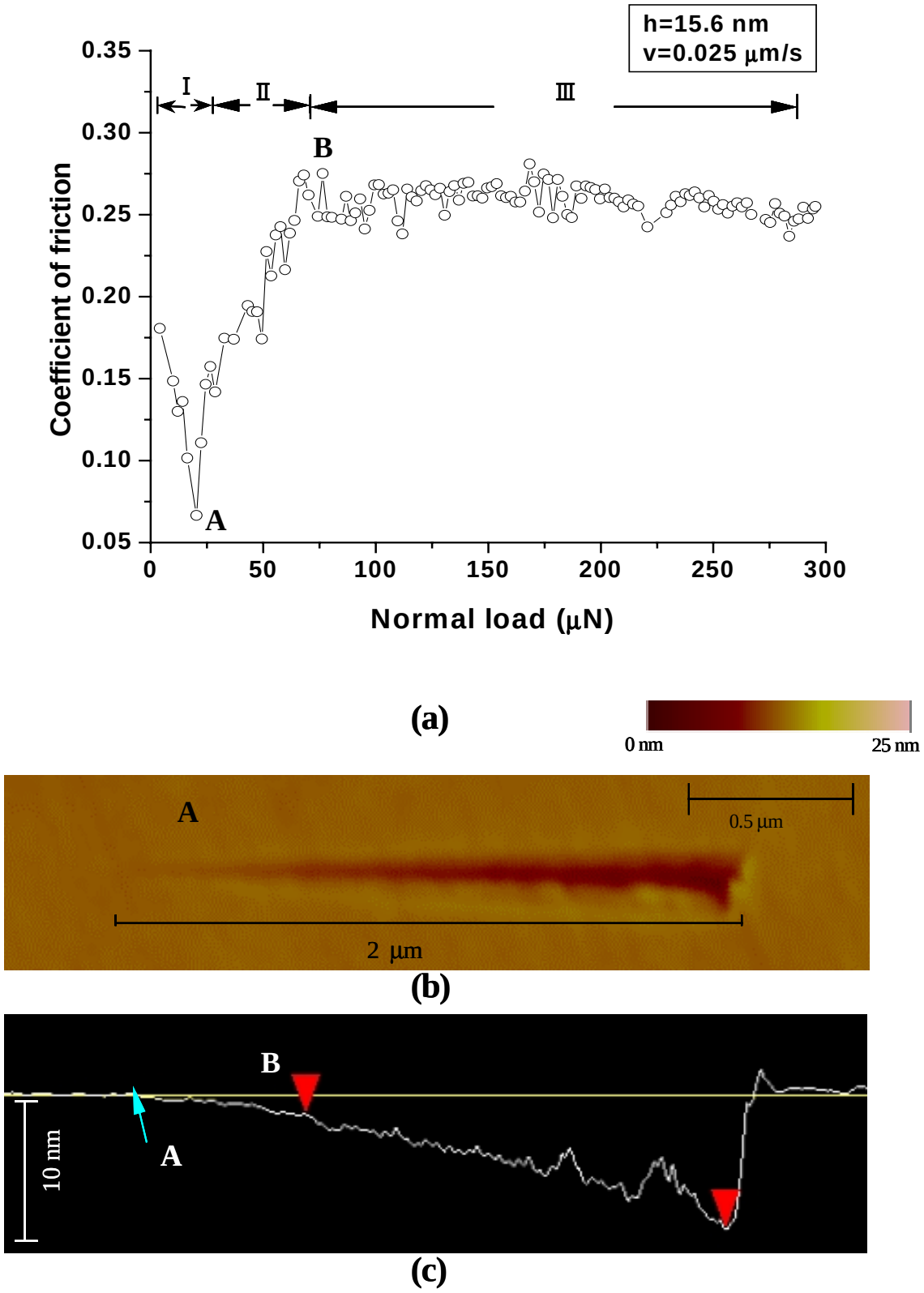

Fig. 3. (a) Friction coefficient versus normal load for 15.6 nm thick film, (b) SFM image of scratched film surface, and (c) cross-sectional view of residual depth profile.

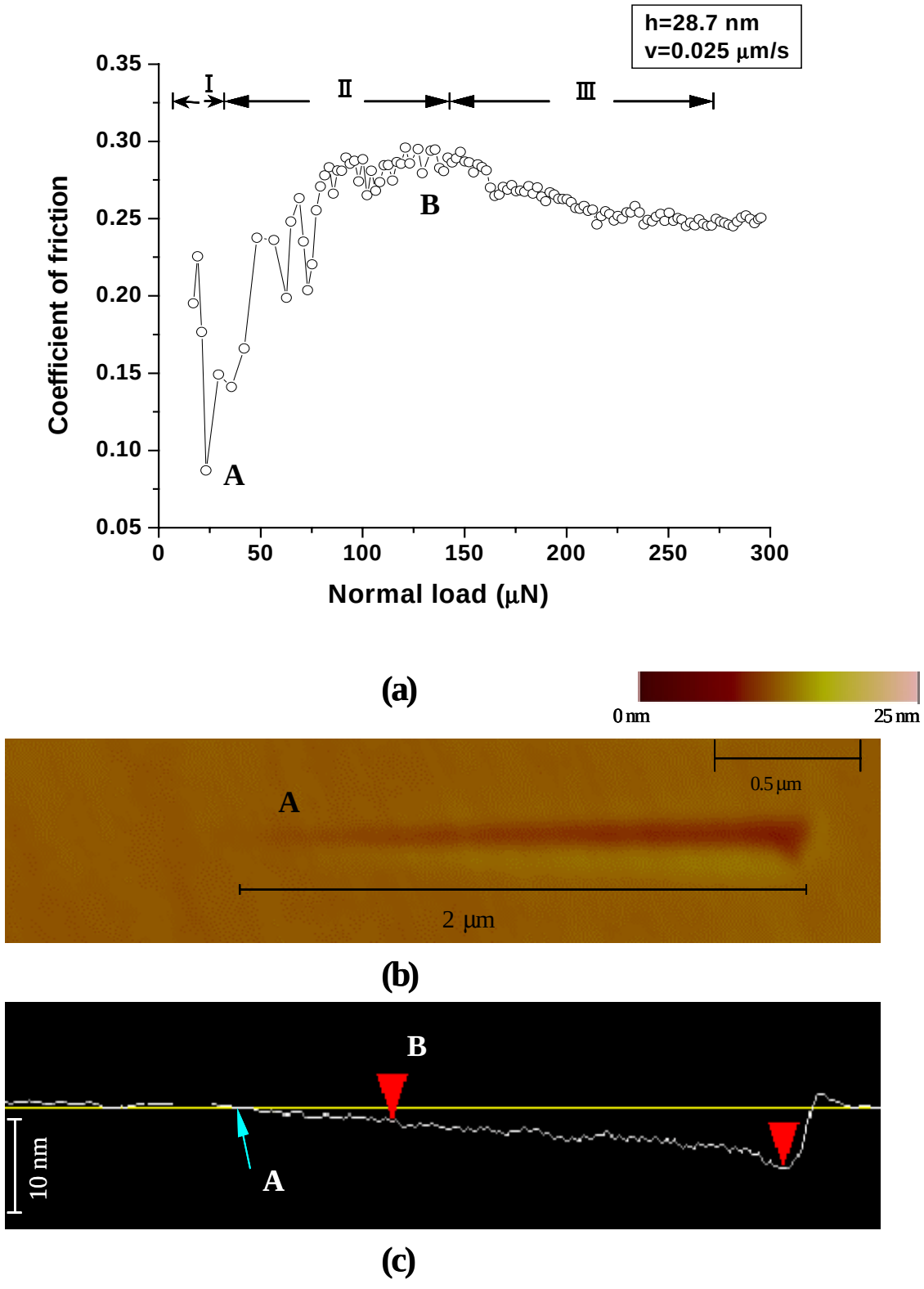

Fig. 4. (a) Friction coefficient versus normal load for 28.7 nm thick film, (b) SFM image of scratched film surface, and (c) cross-sectional view of residual depth profile.

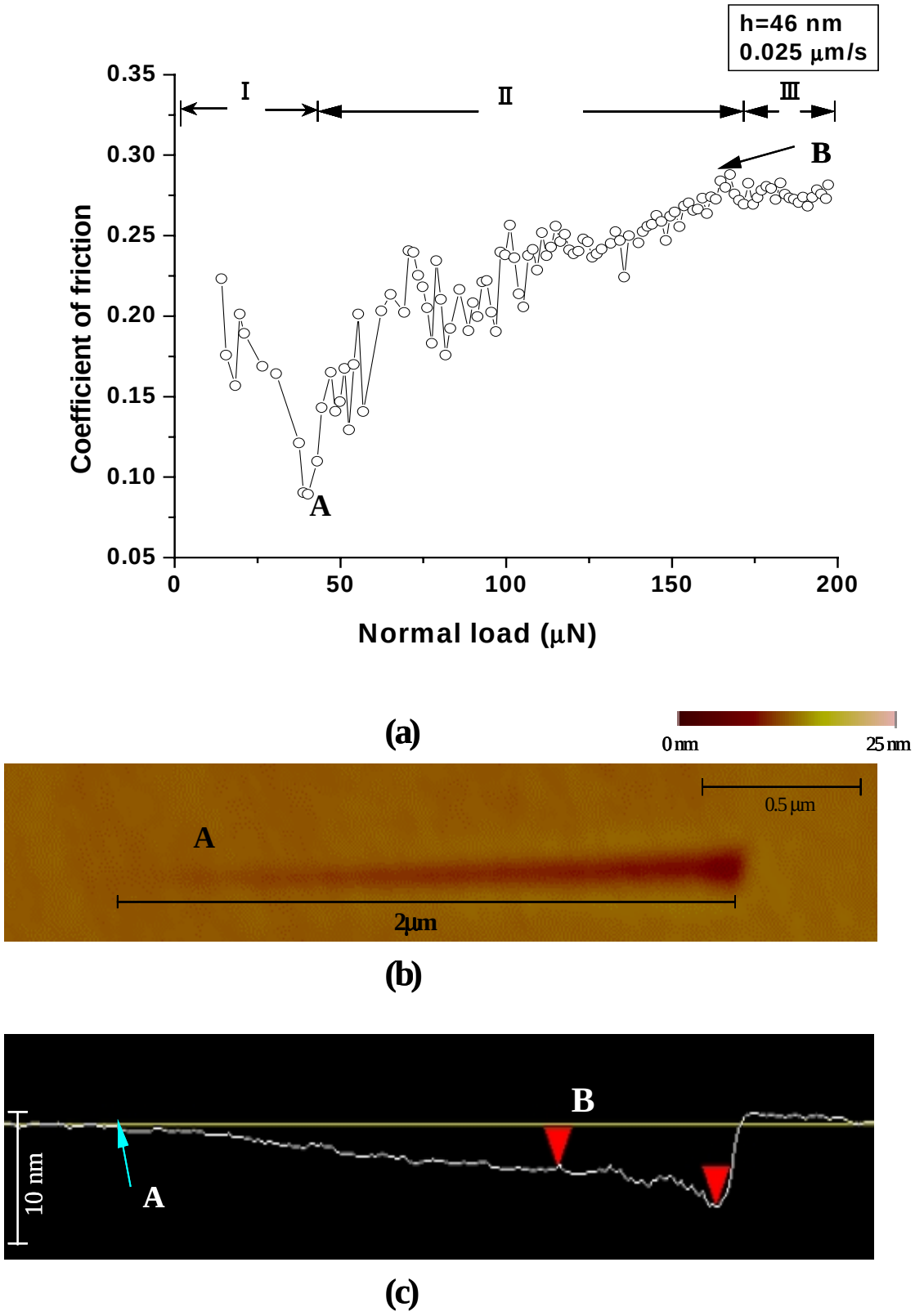

Fig. 5. (a) Friction coefficient versus normal load for 46 nm thick film, (b) SFM image of scratched film surface, and (c) cross-sectional view of residual depth profile.

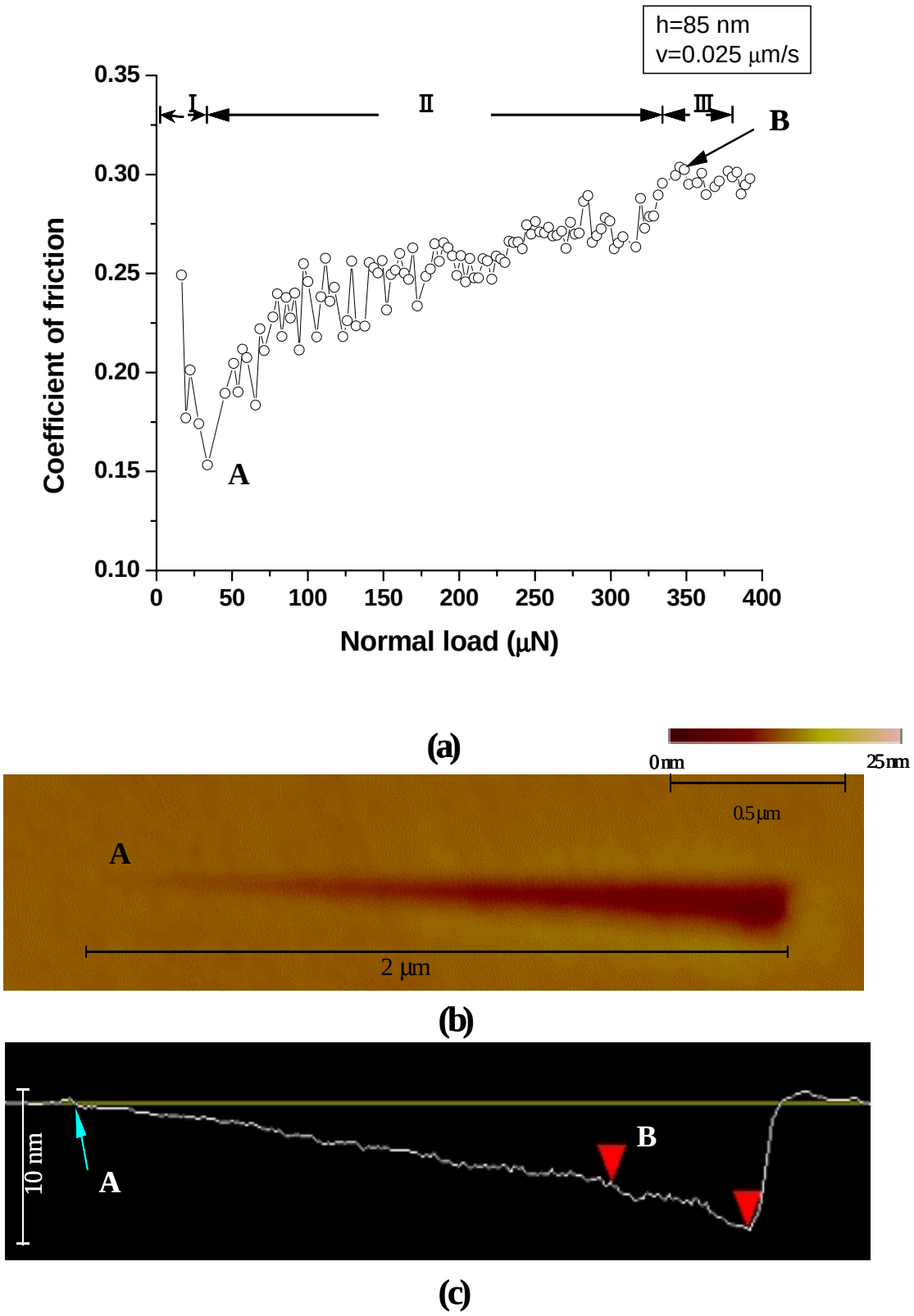

Fig. 6. (a) Friction coefficient versus normal load for 85 nm thick film, (b) SFM image of scratched film surface, and (c) cross-sectional view of residual depth profile.

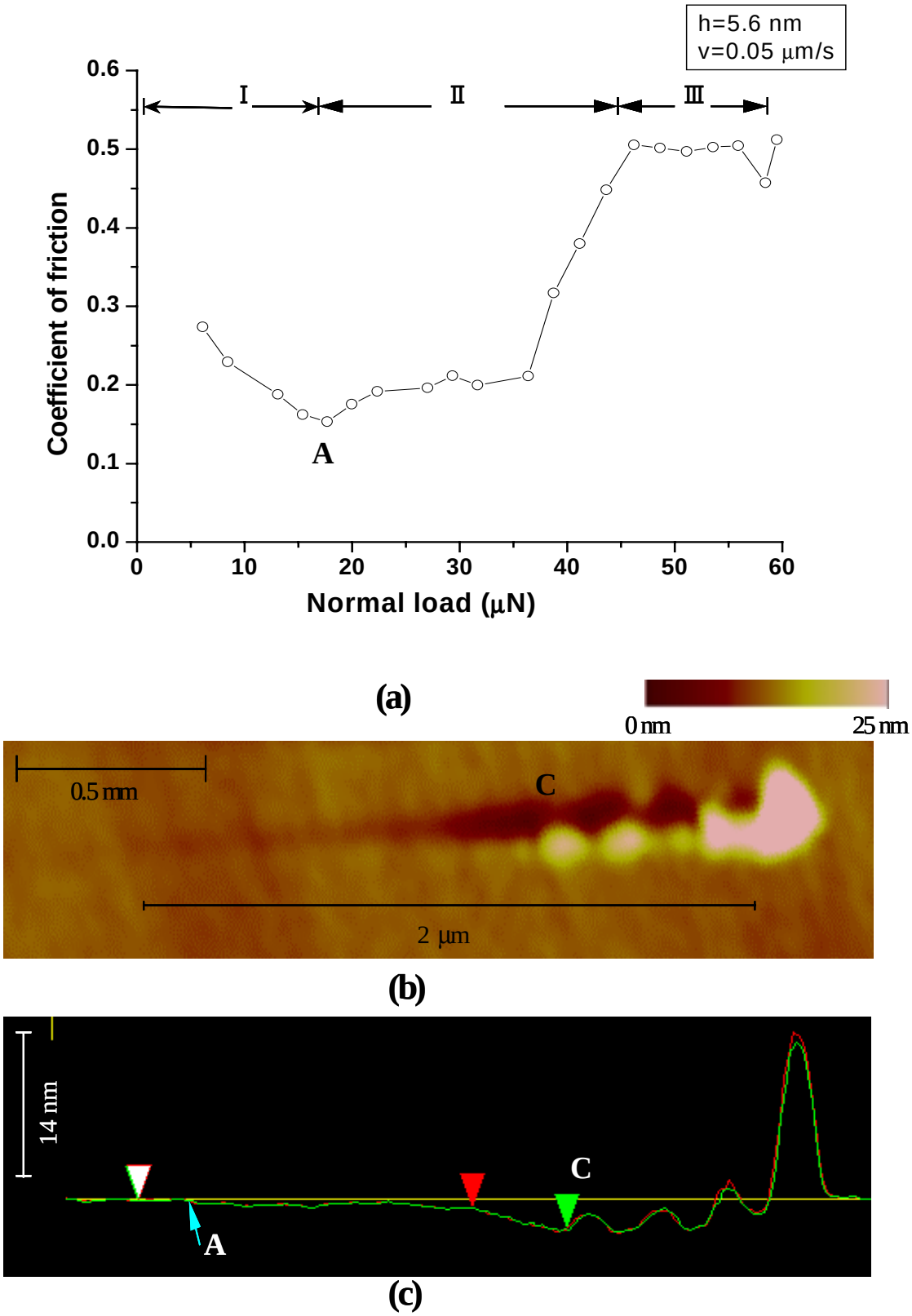

Fig. 7 (a) Friction coefficient versus normal load for 5.6 nm thick film, (b) SFM image of scratched film surface, and (c) cross-sectional view of residual depth profile.

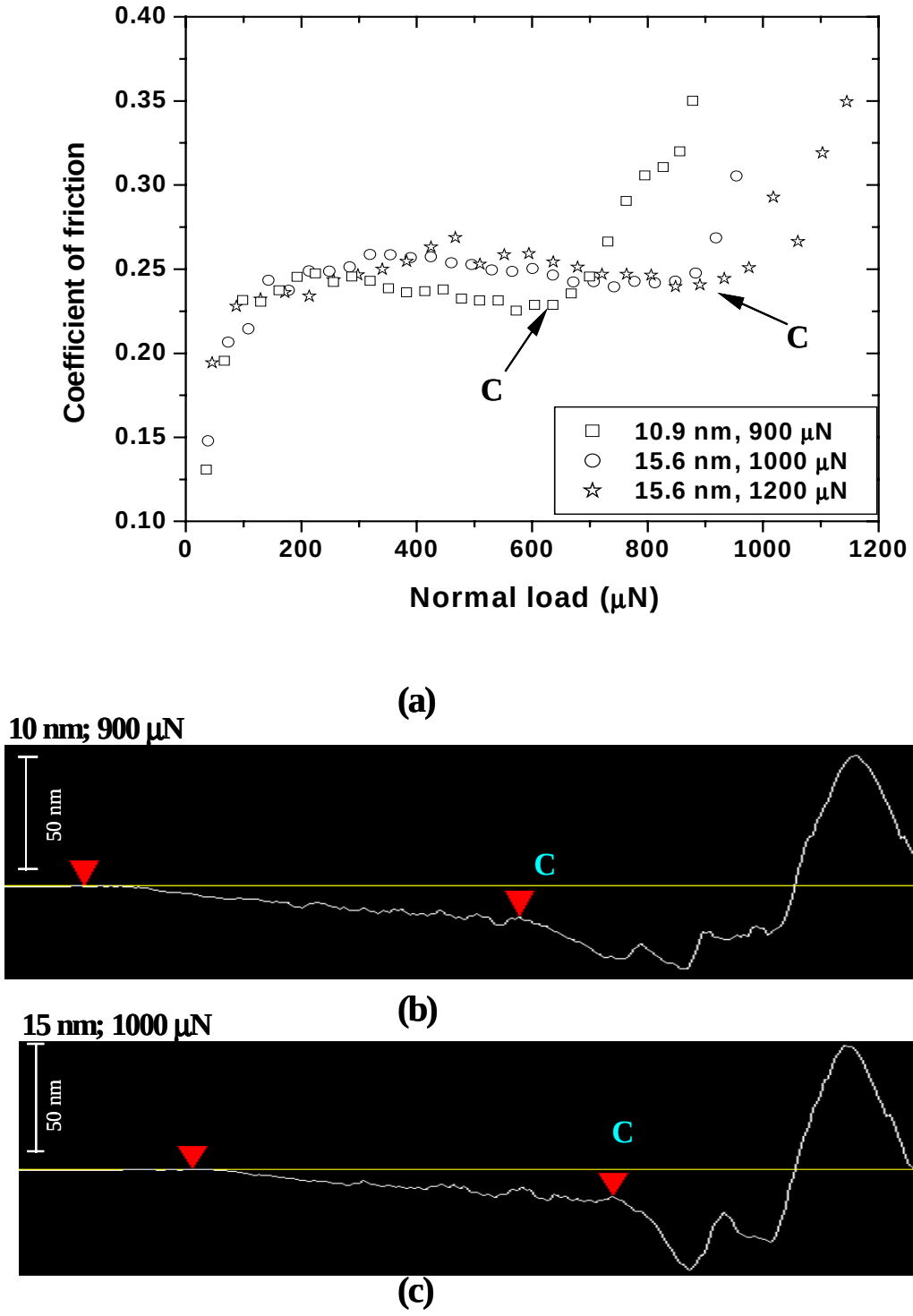

Fig. 8. (a) Friction coefficient versus normal load for 10.9 and 15.6 nm thick films, (b) SFM image of scratched surface of 10.9 nm thick film, and (c) SFM image of scratched surface of 15.6 nm thick film.

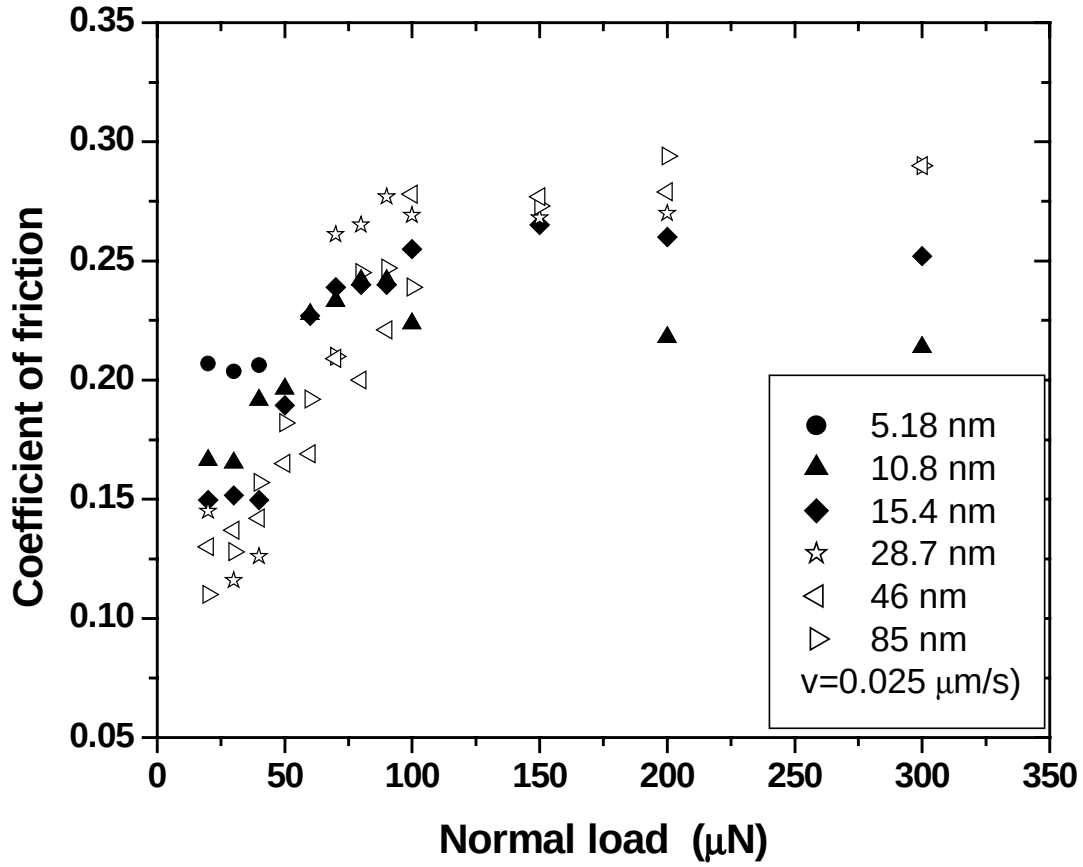

Fig. 9. Variation of coefficient of friction with normal load and film thickness. (Data points represent mean values. The error range in the friction coefficient is less than 0.04)

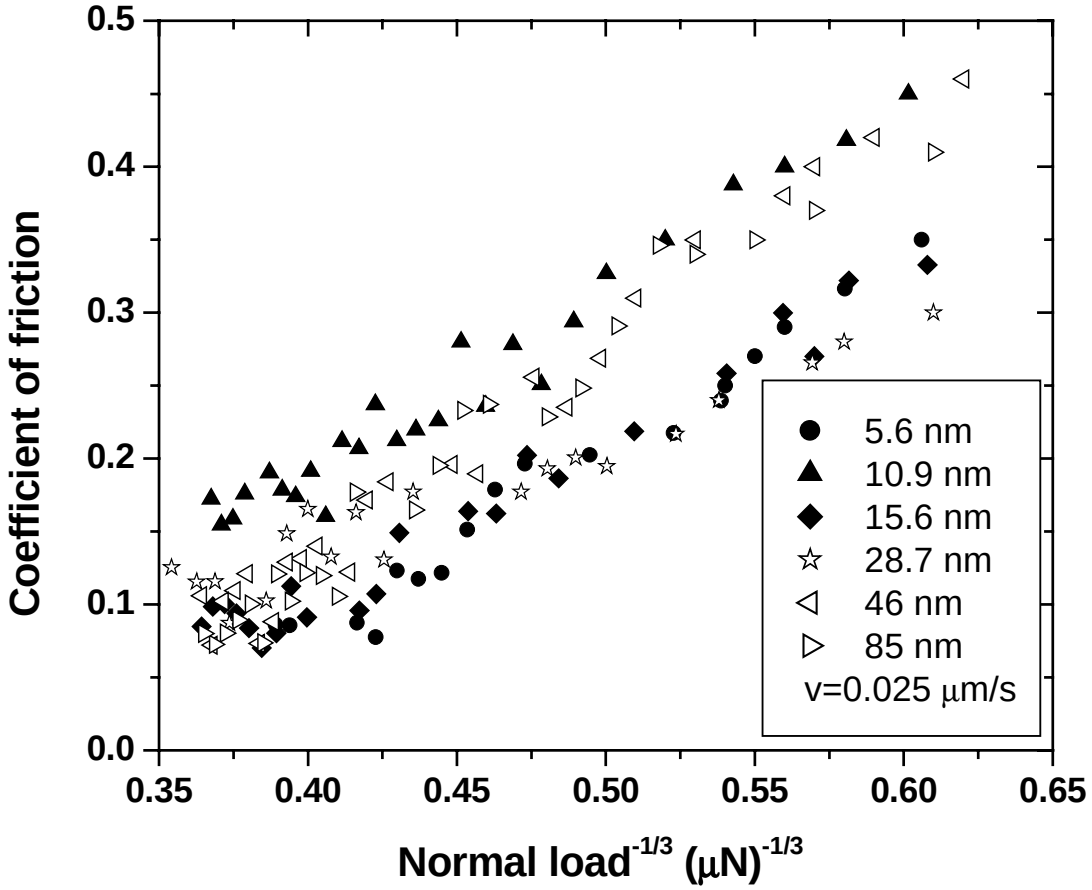

Fig. 10. Variation of coefficient of friction with normal load and film thickness in the low-load range for early stage of scratching.

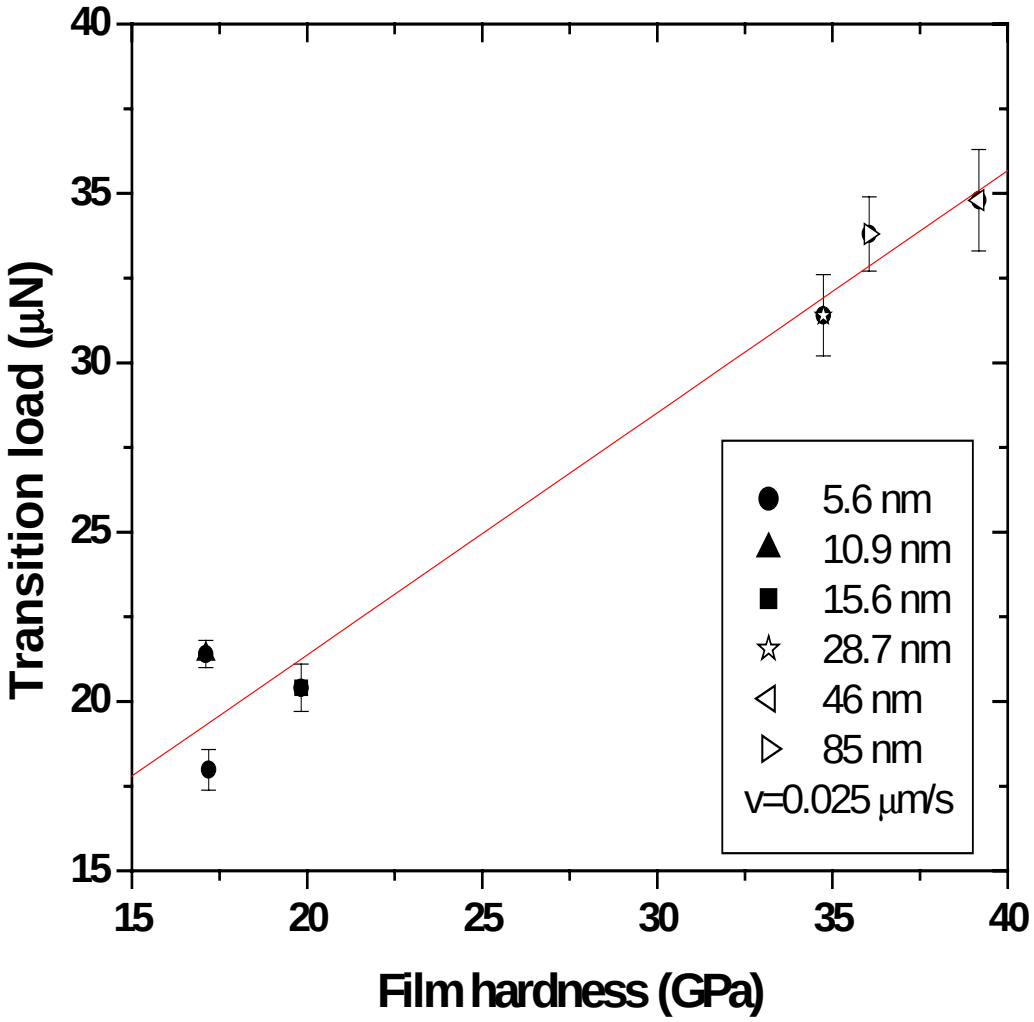

Fig. 11. Transition load versus film hardness and thickness.

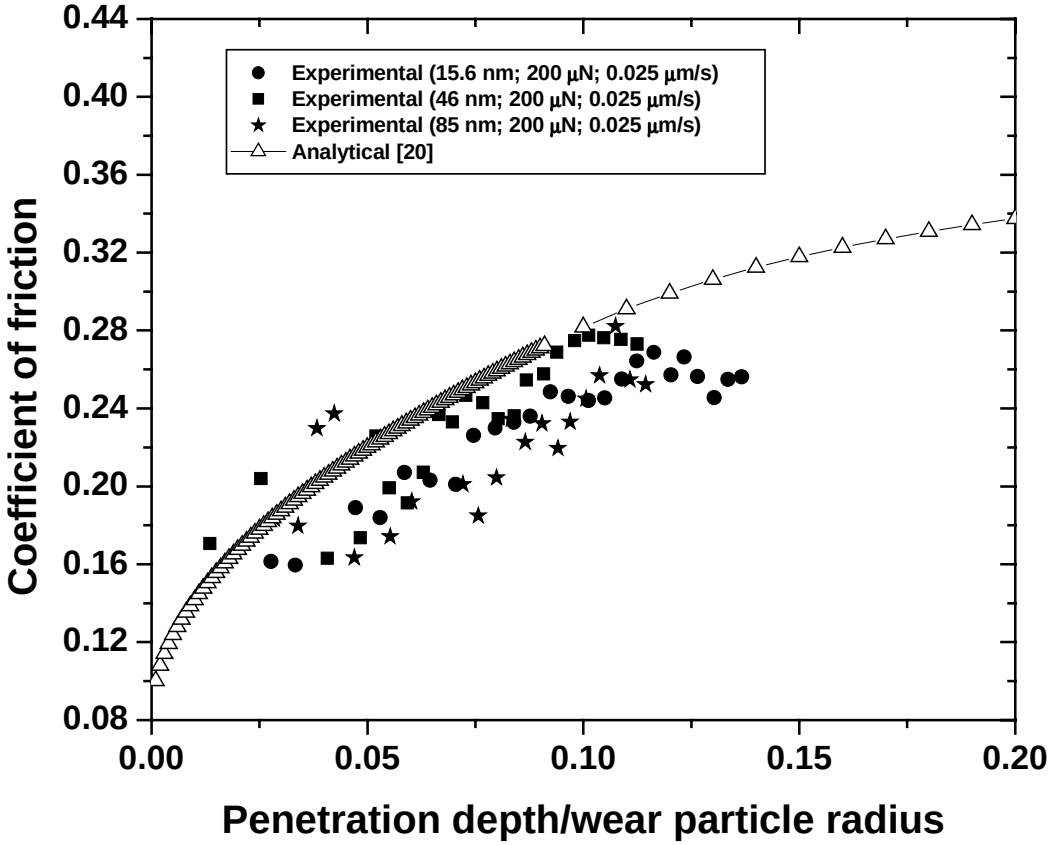

Fig. 12. Comparison of experimental and analytical [20] coefficient of friction results for intermediate load range.